Sensor Testing System for Design of a Quad-Winged Micro Air Vehicle

Final Report

Grant 08NL482

PIs: Haibo Dong and Yan Zhuang

Wright State University

Dayton, OH

August 2010

Report Documentation Page

Public reporting burden for the collection of information is estimated to average 1 hour per response, including the time for reviewing instructions, searching existing data sources, gathering and maintaining the data needed, and completing and reviewing the collection of information. Send comments regarding this burden estimate or any other aspect of this collection of information, including suggestions for reducing this burden, to Washington Headquarters Services, Directorate for Information Operations and Reports, 1215 Jefferson Davis Highway, Suite 1204, Arlington VA 22202-4302. Respondents should be aware that notwithstanding any other provision of law, no person shall be subject to a penalty for failing to comply with a collection of information if it does not display a currently valid OMB control number.

1. REPORT DATE	2. REPORT TYPE	3. DATES COVERED
31 AUG 2010	**Final**	**01-06-2009 to 31-05-2010**

4. TITLE AND SUBTITLE	5a. CONTRACT NUMBER
SENSOR TESTING SYSTEM FOR DESIGN OF A QUAD-WINGED MICRO AIR VEHICLE	**FA9550-09-1-0460**
	5b. GRANT NUMBER
	5c. PROGRAM ELEMENT NUMBER

6. AUTHOR(S)	5d. PROJECT NUMBER
HALBO DONG; YAN ZHUANG	5e. TASK NUMBER
	5f. WORK UNIT NUMBER

7. PERFORMING ORGANIZATION NAME(S) AND ADDRESS(ES)	8. PERFORMING ORGANIZATION REPORT NUMBER
WRIGHT STATE UNIVERSITY ,3640 COLONEL GLENN HWY ,DAYTON,OH,45435	**; AFRL-OSR-VA-TR-2011-0231**

9. SPONSORING/MONITORING AGENCY NAME(S) AND ADDRESS(ES)	10. SPONSOR/MONITOR'S ACRONYM(S)
OFFICE OF NAVAL RESEARCH, 875 NORTH RANDOLPH STREET, ONE LIBERTY CENTER, ARLINGTON, VA, 22203	11. SPONSOR/MONITOR'S REPORT NUMBER(S)
	AFRL-OSR-VA-TR-2011-0231

12. DISTRIBUTION/AVAILABILITY STATEMENT
Approved for public release; distribution unlimited

13. SUPPLEMENTARY NOTES

14. ABSTRACT
A sensor testing system for sensing. control, and modeling of a quad-winged Micro Air Vehicle (MA V) has been built htlhls work. This system contains two Important components. One Is an Agllenl AFM system for microscopic static force measuremcnl and calibration of the scnsor system and another onc Is a Pholron high-speed phologrammetry system for macroscopic dynamic motion-force measurement and vcrlOcatlon, The unique capability of combining ArM and high speed camera has been shown It can provide Information covering from slaUc to dynamic, from microscopic 10 macroscopic for flapping flight study and sensor research. It forms a close-to?real platform to study the flapping ntghl aerodynamics, to exam the flight condition Visually, and to pave the road for the conlrol of agile flIghts.

15. SUBJECT TERMS
SENSING, AFM, HIGH-SPEED PHOTOGRAMMETRY, FLAPPING-WING, MAV

16. SECURITY CLASSIFICATION OF:			17. LIMITATION OF ABSTRACT	18. NUMBER OF PAGES	19a. NAME OF RESPONSIBLE PERSON
a. REPORT **unclassified**	b. ABSTRACT **unclassified**	c. THIS PAGE **unclassified**	**Same as Report (SAR)**	**27**	

Contents

I.   Objectives

The primary objective of the proposed research is to build a sensor testing system for verification, calibration, modeling of the senor design for sensing, control, and modeling of a Quad-Winged Micro Air Vehicle. Two equipments will be used for measuring the static force of the wing and recording time-resolved deformation of wing in dynamic motion respectively. They are consisted of a Agilent-5420 AFM System and Photron 1024 PCI High-Speed Camera system. This provides a close-to-real platform to study the aerodynamics with small Reynolds number, and to exam the flight condition visually to eventually realize the control of the agile flight. The coherent study on coordination of sensing, date-processing, and actuating, we believe, is the core knowledge and technology for future MAVs.

The other objective is to serve more DoD projects to develop new research capabilities to support research in the technical areas of interest to the DoD. Based on the purchased equipment, we explored the research into bio/chemical-sensing, characterization of single atomic layer graphene, nano-granular ferromagnetic materials/ferrites for integrated RF passives, GaN based power electronics, and micro-batteries.

II.   Status of Effort

In the past year, the system supported a few DoD projects: 1) Deployable Low Power Carbon Nanotube Sensors (AFRL-FA8650-09-1649), 2) Developing spin coated ferrites for on-chip RF applications (ONR-N000140710761 and N000140810526). The system also triggered a number of collaborations with Wright-Patterson air force base including 1)) RF characterization of graphene films on SiC substrate, 2) Surface morphology characterization of nano-granular ferromagnetic thin films for integrated RF passive components. The system has also been widely used as a research/teaching platform to train both under- and graduated students in the fields of micro aerial vehicle, sensing, actuator, RF characterization, and nano technologies, which strongly enhance the research/education capability at Wright State University. It becomes a major instrument in the Microsystem and Microwave laboratory, serving a large number of courses: EE410, EE442, EE446, EE480, and EE440.

In addition, a number of proposals have been submitted to various DoD programs during the past year to extend and develop new research capability based the purchased equipment:

1. Phase II - Sensing, Control and Modeling for a Quad-Winged Micro Air Vehicle Platform (Air Force STTR, F2-1747).

2. Magnetic materials with strong ferromagnetic precession properties and low damping, N102-167-0477 (ONR-SBIR)

3. MEMs based thermopile infrared detector array for chemical and biological sensing, A10A-004-0311 (Army – STTR 2010)

4. Advanced thermoelectric Milli-Power Source, A102-094-1626 (Army SBIR 2010)

5. Flow Modulation and Force Control of Flapping Wings, AFOSR 2010.

A few more proposals are planned to submit:

A11-015　　　(Army SBIR 2011) - Direct Sensing of Micro Unmanned Aerial Vehicle Lift

III.　　Accomplishments and New Findings

A. Atomic force microscopy

The system purchased is a multiple user research system for atomic force microscopy (AFM) and scanning probe microscopy (SPM), including scanning tunneling microscopy (STM), Kelvin force microscopy (KFM), electrical force microscopy (EFM), and magnetic force microscopy (MFM). AFM is often called the "Eye of Nanotechnology", i.e. a high-resolution imaging technique that can resolve features as small as an atomic lattice in the real space.

The Agilent 5420 provides a wealth of unique technological features in electrical characterization capabilities with nanometer scale spatial resolution. The system has broad applications in electrochemistry, material science, polymer science, nanolithography, nanografting, life science, biotechnology, and semiconductor materials and devices. It offers characterization of

1) Surface morphology
2) Local electrical polarization
3) Surface electrochemistry potential
4) Imaging of atomic lattice
5) Magnetic domain
6) Materials' electromagnetic property at radio frequency

B. Modification of AFM to scanning wave microscopy

Supported by the other grant, we purchased Agilent vector network analyzer N5230C (PNA-L). The PNA is capable to perform radio frequency characterization up to 40 GHz. In this phase of the project, we successfully combined the AFM and the PNA, enabling the local RF characterization with spatial resolution down to nano meter range. Such a system provides an unique function to perform calibrated electrical measurements by the PNA with the outstanding spatial resolution of an atomic force microscope. The modified system outperforms traditional AFM-based scanning capacitance microscopy techniques, offering far greater application versatility, the ability to acquire quantitative results, and the highest sensitivity and dynamic range in the industry. This allows us not only perform DC-static measurement, but also RF/microwave measurement at nano-scale. WSU is the 1st university national wide equipped with such system, and is the only one capable of performing SMM measurement in Ohio. The

equipment enhanced significantly the research capability of our department on nano-materials, sensors, and microwave technology.

C. Built a High-Speed Camera System for Flapping Flights

The most important component of our high-speed photogrammetry system is the camera itself. We use 3 High-speed Cameras aligned along the principle coordinate axes (Figure 1). For our system, we chose the Photron Fastcam SA3 60k model. This camera is a CCD sensor with 17um pixels. The system is capable of capturing a maximum of 1000 black and white frames per
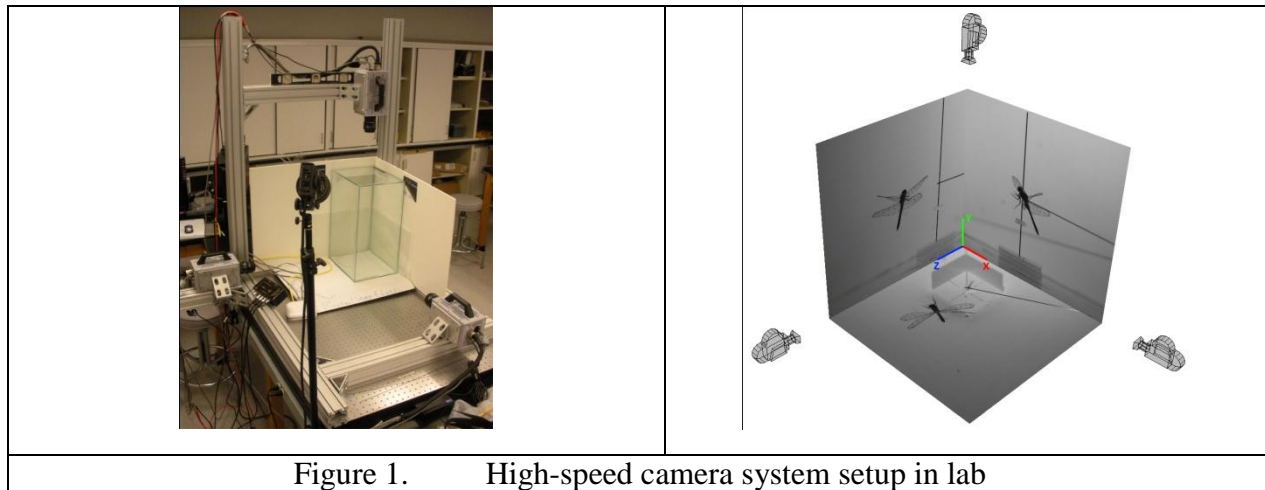

Figure 1.   High-speed camera system setup in lab

second at full resolution (1024x1024) with a global shutter speed of 2 us. With 4 Gb of onboard storage, this stand-alone, network-attached camera system allows for a maximum record time, at optimum settings, of 2.726 seconds.

The camera system was designed with adaptability in mind. Another major component of our system is the foundation. The foundation and framework that supports the three cameras is comprised of an optical breadboard and extruded aluminum profile. For the optical breadboard we chose a Newport 4'x4' platform with ¼-20 mounting holes and is true across the surface within 0.001". This was paired with 8020 4"x4" Extruded Aluminum Profiles with the appropriate proprietary mounting hardware. The slotted channels in the aluminum supports allows us to provide quick coarse adjustment to the camera positions while ensuring that we maintain perpendicular positions from each camera perspective. The optical breadboard allows us to mount our hardware to a sturdy anchor and ensure that minimal vibrations will occur within the system.

We use a standard array of lenses that are commonly used in commercial photography applications. The lenses we use are Nokia F-Mount lenses with a fixed focal length. These lenses allow us to utilize our full sensor without vignetting occurring in our image. Vignetting is a form of optical distortion that reduces image clarity on the edges of the image in comparison to the center of the image. The fixed focal length or the lenses ensures that we will see a comparable amount of perspective distortion in each camera. All lenses have a low F-number or focal ratio.

5

This is the comparison of pupil diameter of the lens with the focal length. The lower the f-number is, the more light is allowed to be exposed to the sensor. This is a very important characteristic to take into consideration for this type of system. To capture high-resolution, high speed images of objects that are moving at a high-speed, the exposure must be adjusted to compensate for this motion. One way of compensating for motion blur is to move the cameras in sync with the subject. However, because of the static configuration of the cameras, this is not possible, and only one degree of freedom is available to compensate for blur: shutter speed. Because of the minimal global shutter or our cameras, we can increase the shutter speed and capture crisp images. In doing so, less light is allowed to interact with the CCD sensor, so our optics must allow as much light in as possible. Another aspect of optics that is utilized is the aid of extension tubes. Extension tubes increase the distance that the optics are from the body of that camera. In doing so, we can affect the amount of magnification the lens will have. As the distance of the lens from the sensor increases, the image will appear larger. This can be helpful in adding more detail to certain areas of investigation, such as wing actuation or in the application of mechanism analysis, failure and fatigue zones. By using extension tubes, however a great deal of light and depth of field is lost in the final image. So extension tubes are used for very specifics investigations.

The camera system once installed and configured with any standard personal computer, is capable of being synchronized and triggered simultaneously. For this task, we use a daisy-chain method to loop the cameras to one another. Because the cameras, much like many professional photography set-ups, are triggered by an external Transistor-Transistor Logic (TTL) signal. By configuring the cameras in a master-slave arrangement, it is possible to trigger one camera to relay the signal to the other two cameras. By using this method of triggering, we are capable of minimizing camera delay and maximizing the response time. This lag between timing in sequential frames can be a major hassle during post-processing, so the goal of this system is to minimize the delay between cameras. Our current measurements indicate our delay between cameras at a maximum of 30 nanoseconds, which for our applications can be taken as zero delay between frames.

A key aspect to any form of photography is lighting. For our purposes we need as much light in the scene as possible so that motion blur and loss of light from extension tubes can be compensated for. We achieve this amount of lighting by using Lowel Focus Floodlights with a maximum of 250 Watts of power across two lamps that are outfitted with tungsten bulbs. These lights provide a clean, reliable glow that floods the entire scene with ample amount of light. Because the lamps do give off a fair amount of heat, the lighting system is kept further away from the insects to ensure that the heat does not affect the insects' flight performance.

The camera system can be trigged using three distinct modes: start, center, and end trigger. Because the cameras are stand-alone systems, they can continuously save data within their onboard memory. This allows us to save data post and pre trigger. In doing so, we can ensure that the subject being filmed has some buffer time to allow it to remain in focus for the

maximum time allotted. This is very helpful in collecting crisp, well-focused data. We can use this feature in combination with a system we designed to allow hands-free triggering: the laser trigger system.

The laser trigger system is a custom designed circuit that uses the open-source Arduino microcontroller platform to control our cameras. We use common laser diodes to provide focused beams of light to opposing light sensitive resistors. At the intersection of these two laser beams, we are able to focus our cameras, so that when a free flying insect breaks both beams simultaneously, the microcontroller will give an output trigger signal to our cameras. This system removes all human error associated with the cameras. By allowing the system to detect when the subject is in optimum range of photography, we can collect more accurate data.

Because our camera systems use onboard memory as opposed to some PCI systems, we are able to store multiple data sets on our cameras before removing the data for post processing. By using the cameras' auto-partition system, we are able to generate 8 equally spaced partitions with a maximum of 0.304 seconds of flight data per partition. Once the laser trigger system has detected 8 events where the insect is in the appropriate focal range of the cameras, the data is automatically stored and can be set to auto-download to the appropriate directories with the appropriate file extensions and naming conventions. This allows us to collect large volumes of highly accurate data with a great deal of automation, which speeds up the entire data collection process. This means that less time of filming is required to collect the necessary amount of data; so the insects are exposed to less heat from the lamps and suffer fewer injuries caused by collisions with the tanks in which they are filmed. This means that our insect subjects can have more useful data collected during their lifespan as opposed to a manual trigger system which would require a lot more guesswork and time to film the subjects.

D. Data Collection Process Using the High-Speed Camera system
The cameras are calibrated using a series of calibration matrices. By taking images from the cameras of a calibration object with a set of given points with known dimensions, we are able to decomposed the camera properties into a P-Matrix. The P Matrix is composed of the camera calibration properties as well as translational and rotational components. The process for collecting this data is described by [9]. Once one camera has been calibrated and the given P matrix has been formed, we are able to use these specifics to decompose the 3 dimensional global coordinate system into a two dimensional image plane. By performing the calibration for all three cameras in the system and calculating three separate P matrices, we are able to create associated two dimensional image planes that can be combined, in reference, to reconstruct the motion of the objects in the global three dimensional coordinate system.

Many difficulties arise during the data collection process that was only made evident in the post processing of the data. One of the minor difficulties we faced during the post processing h as already been mentioned in this paper. The cameras are delayed from frame to frame by a small variation. Although some of this can be corrected using aftermarket animation software, it is

impossible to completely overcome this difficulty. Like with any system, nothing can be completely efficient, and this is something that we are currently trying to minimize for future use.

Another complexity that we had to address in post processing was the depth of field of our images. Because we are focusing on the object from a very small working distance (less than one meter) our image field depth tends to be quite shallow. In the case of dragonflies, the depth of field equates to around two body lengths. This provides some difficulties in reconstruction. Because the insect is in focus for such a short distance, full surface reconstructions with true deformation in the wings is only able to be performed for several wing beats. However, for less detailed flight analysis such as flat plat simulated wing motion and body vertex tracking, less detail is required and more wing beats can be analyzed.

Because of our increased shutter speed and use of extension tubes in some case, we had to flood our scene with a great deal of light. An insect's wings are membranous and often iridescent and reflective. This causes glare to form in some images when the wing surface reflects light into the camera. This can make it very difficult to see the wing surfaces. We are able to overcome this difficulty by marking a grid like pattern of dots across the surface of each wing. This uniform pattern serves as a reference for reconstructing the wing. Because the wings were marked with a fine tipped permanent marker, the added weight from the ink on the surface of the wing is approximated as zero, and does not affect the flight performance of the insect. By calibrating all three camera viewpoints we can reference from multiple views during the reconstruction process. We found that when parts of the wings were obstructed in one view, that the other two views provided sufficient clarity and detail for reconstruction.

The largest complication came from capturing true free flight motion of the insects. Because we intended to capture motion of the insects from non tethered data, we had to develop a system that allowed us to capture the flight data when the insect was in the focus range of the cameras. The insect subjects were very uncooperative at first. To ensure that the insects were not provoked into flight or restricted in any way possible, we used the laser trigger system to automate our data collection. This allowed us to capture only the usable data of our insects without having to manipulate the insects' flight paths.

E. **Results And Findings**

1. **Design/Fabrication of silicon based ultra-sensitive pressure sensors**

l) Design of ultra-sensitive pressure sensors

Design and processing of ultra-sensitive flow sensor goes to the very heart of the proposal. We completed the mask layout design of ultra-sensitive pressure sensors (Fig. 2). Totally 5 masks with 264 pressure sensors with various geometrical configurations were designed.

<table>
<tr><td>(a)</td><td>(b)</td><td>(c)</td></tr>
</table>

Figure 2. Mask layout with various magnification factors.
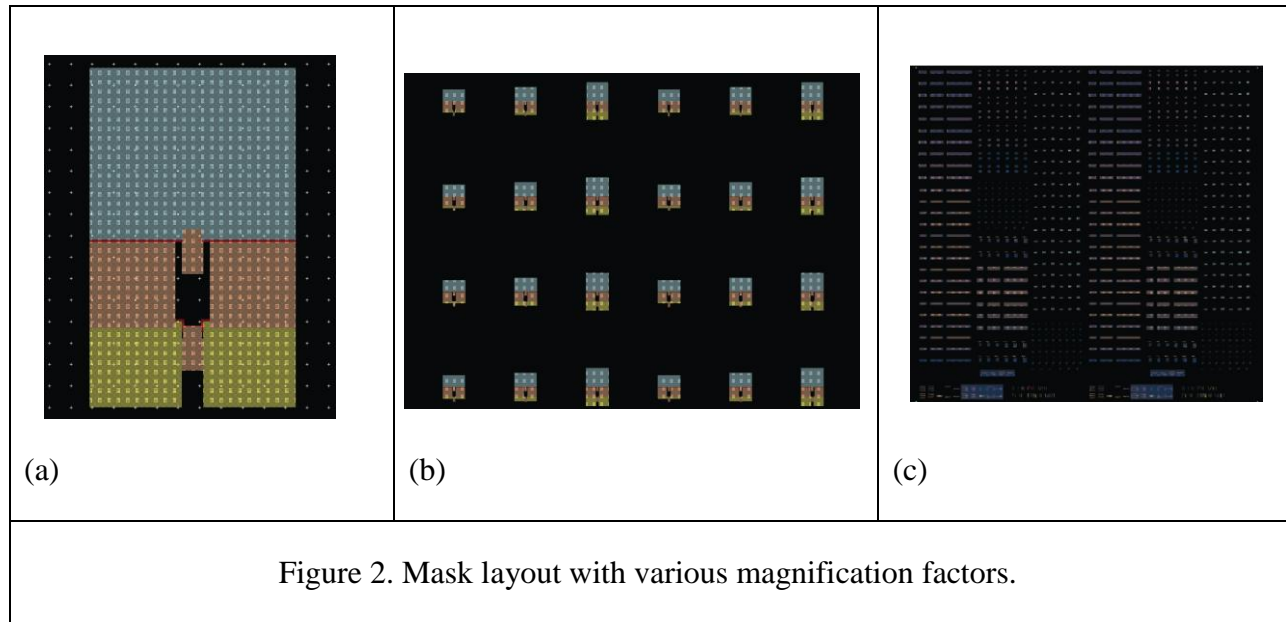
II) Processing flow design of ultra-sensitive pressure sensor

The processing contains 5-masks:

1) Substrate selection
   The processing starts from a SOI substrate. The top Si-layer is n-type Si (001) with thickness 500nm.

2) Deposition of 100nm-thick SiO_2 layer

3) Formation of p-well
   Mask: piezo_resistor_01
   Step 1: Dry-etching 100nm SiO_2
   Step 2: Boron doping - concentration $10^{18}cm^{-3}$ (implantation or diffusion)
   Step3: Drive-in and annealing

4) Remove the surface SiO_2 by wet-etching

5) Fabrication of Si cantilever
   Mask: piezo_resistor_02
   Step 1: Dry-etching Si and stop at the buried oxide layer

6) Deposition of 500nm-thick SiO_2 layer

7) Contact window opening
   Mask: via
   Step 1: dry etching through the deposited SiO_2 until the underneath Si is fully opened. Over etching might be needed to assure a good contact.
   Step 2: boron doping 15KeV, dose-$3\times10^{15}cm^{-2}$ (or equivalent diffusion procedure based upon equipment availability)

Step 3: drive-in and annealing

8) Deposition of 2μm Al layer

9) Metallization
   Mask: top_metal
   Step 1: etching the AL layer

10) Deposition of 1μm SiO2 to protect the front side

11) Deposition of 1μm SiO2 to protect the back side

12) Backside KOH etching to release the cantilever
    Mask: sensor_koh (89)
    Step 1: KOH etching of the bulk Si substrate from the back-side of the wafer until to the buried oxide layer

2. **Microwave imaging of graphene oxide and DNA** (AFRL-FA8650-09-1649)
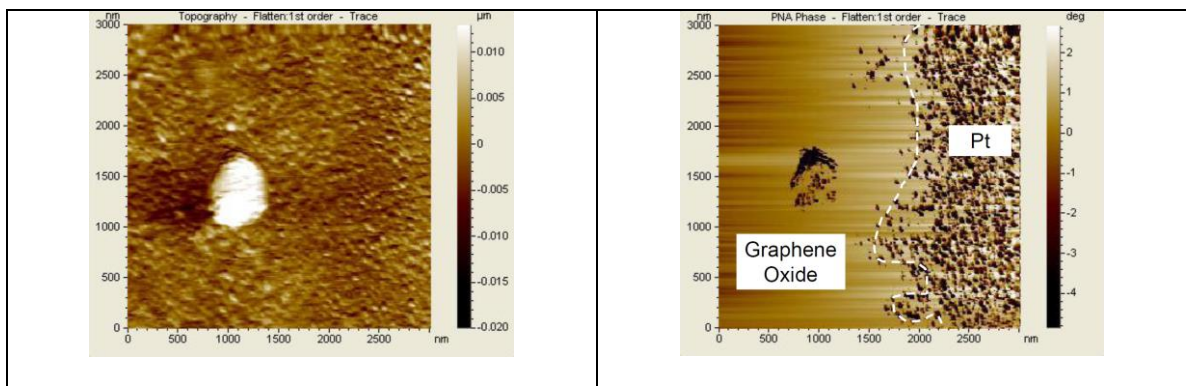

Figure 3. Micrograph of surface morphology by AFM (Left), and impedance (Right) measured at f=2.375538 GHz. Due to the thin thickness of graphene oxide (~1nm), the boundary between graphene oxide and Pt is hardly seen by AFM. Applying RF/microwave signals, the boundary is clearly revealed on the impedance measurements because of the difference of the electrical conductivity between the graphene oxide and platinum.

Graphene is one atomic layer covalent-bonded carbon atoms in a hexagonal pattern, and the building block of carbon nanotubes which has been studied for biosensing extensively. The atomic thick graphene sheet is an ideal material candidate for bio-sensing for the potential of high specificity and up to single atom or molecule detection sensitivity. It may open up a new paradigm in identification and detection of existing or emerging pathogenic micro-organisms, unknown toxins, and viral threat agents.
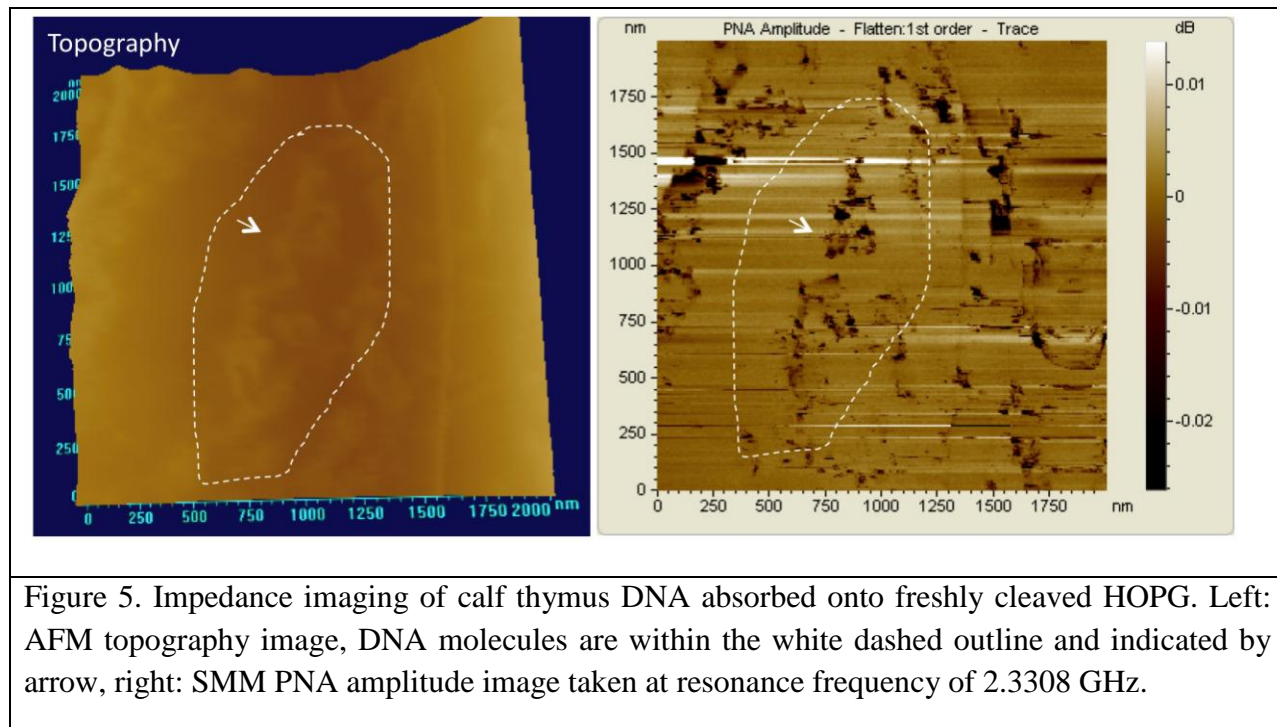
Since experimentally isolated in 2004, graphene has revealed various astonishing properties among all the existing materials, e.g. the highest intrinsic mechanical strength (1060 GPa), the highest thermal conductivity (3000Wm^{-1}K^{-1}), high surface area (2630 m^2/g), high electronic mobility (10000 cm^2/V/s, 100 times faster than in Si). The remarkable carrier mobility at room temperature leading to an extremely low noise level, together with the extremely large surface area and adjustable surface chemistry make graphene excellent candidates for chemical/bio sensing.

Figure 4. Micrograph of graphene oxide on platinum layer at various frequencies.
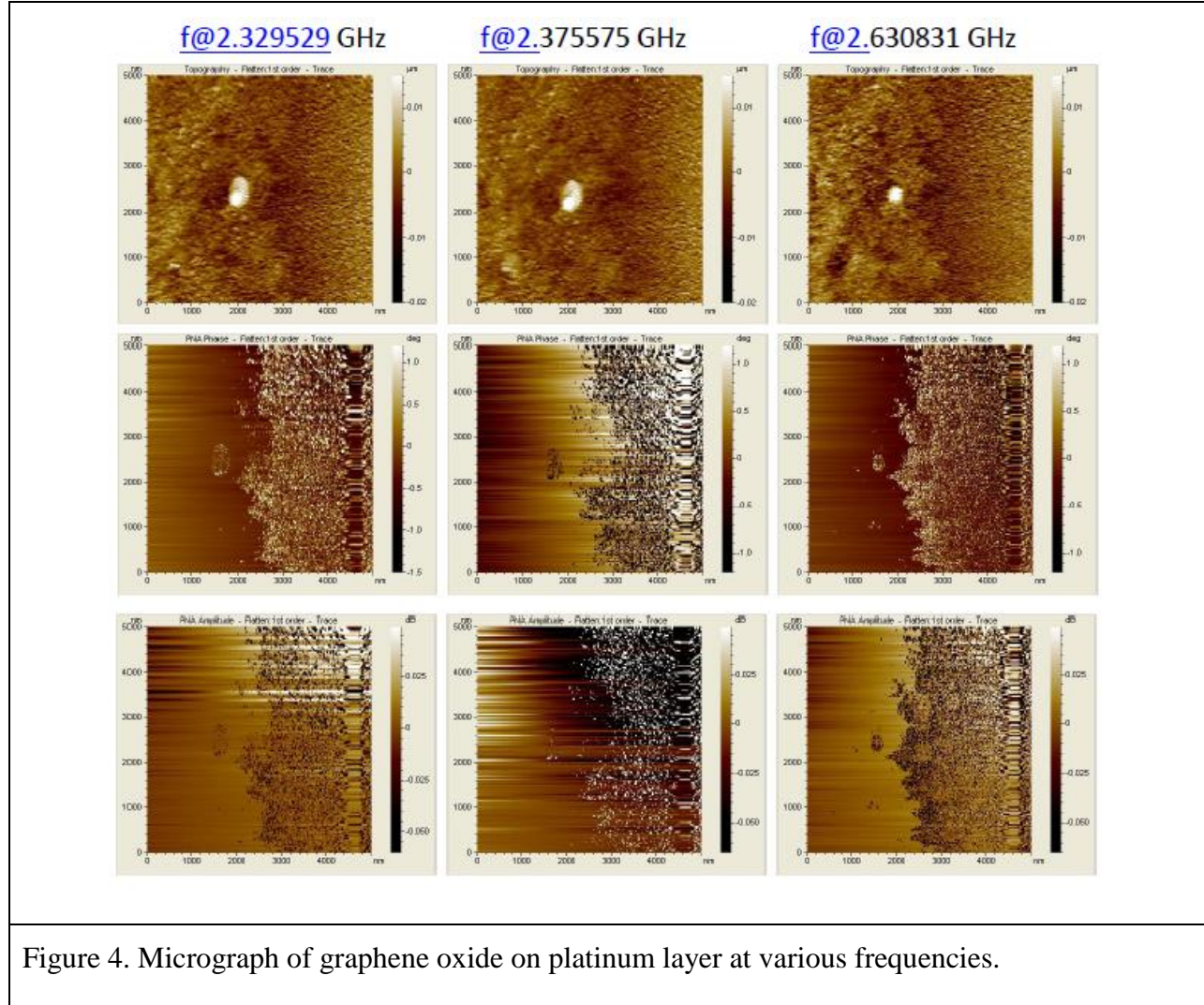
We performed a broadband in-situ RF/microwave (up to 40 GHz) characterization with nanometer scale spatial resolution, by combing atomic force microscopy and RF/microwave network analyzer. In our experiment, tiny amount of graphene oxide (insulating) was placed onto a surface covered with Pt (conductive) nanoparticles. Scanning microwave microscopic imaging (Fig. 4) revealed a clear boundary between the graphene oxide covered area and the uncovered region. Due to the small thickness (~1 nm) of graphene oxide sheets and the relatively rough Pt nanaoparticle (5-6 nm), the same boundary is hardly visible on the topography image. A few

more measurements are shown in Fig. 4, recorded at various frequencies. Both the phase and amplitude show the contrast between the graphene oxide and the platinum under layer.

Additionally, we have prepared calf thymus DNA solution and placed it onto freshly cleaved HOPG for impedance imaging. As expected, we observed clear contrast in impedance amplitude image (Figure 5) caused by the different conductivity of these two materials (HOPG vs. DNA). These results suggested that our system is capable of detecting changes in electronic properties caused by the absorption of other molecules or materials.

Figure 5. Impedance imaging of calf thymus DNA absorbed onto freshly cleaved HOPG. Left: AFM topography image, DNA molecules are within the white dashed outline and indicated by arrow, right: SMM PNA amplitude image taken at resonance frequency of 2.3308 GHz.

3. Spin-Spray Deposited Ferrite/Non-Magnetic Multilayer Films with Enhanced Microwave Magnetic Properties

Bulk microwave ferrite materials have been widely used in RF/microwave devices, which suffer from limited operating frequency (< 600 MHz) under self-bias condition due to the well known Snoek's limit. Magnetic/non-magnetic multilayers have been attracting a lot of attentions for its significantly reduced coercivity, low hysteresis loss, self-biasing, narrow ferromagnetic resonance (FMR) linewidth, low eddy current loss.

In this work, a low temperature fabricated ferrite/non-magnetic multilayers with enhanced microwave magnetic properties has been demonstrated, providing a viable route for achieving thicker ferrite films loading in RF/microwave devices without suffering from degraded

microwave magnetic properties. $Ni_{0.27}Zn_{0.54}Fe_{2.43}O_4$ (NZFO)/Al_2O_3/$Ni_{0.27}Zn_{0.54}Fe_{2.43}O_4$ and single layer NZFO thin films were deposited. Surface topography measurements were performed on the Agilent 5420 and shown in figure. The measurements were imaged using contact force mode. The images were processed with Pico Image to extract the height profile, which is to be used as a measure of surface roughness. The extracted profiles showed that single ferrite layer films and the double layer films had similar morphology as well as surface roughness. The multi-layered films showed very different morphology with big clusters (~ 3 times larger in diameter) of smaller particles and the surface roughness is almost twice as big as the former two. The work supports ONR awards N000140710761 and N000140810526.
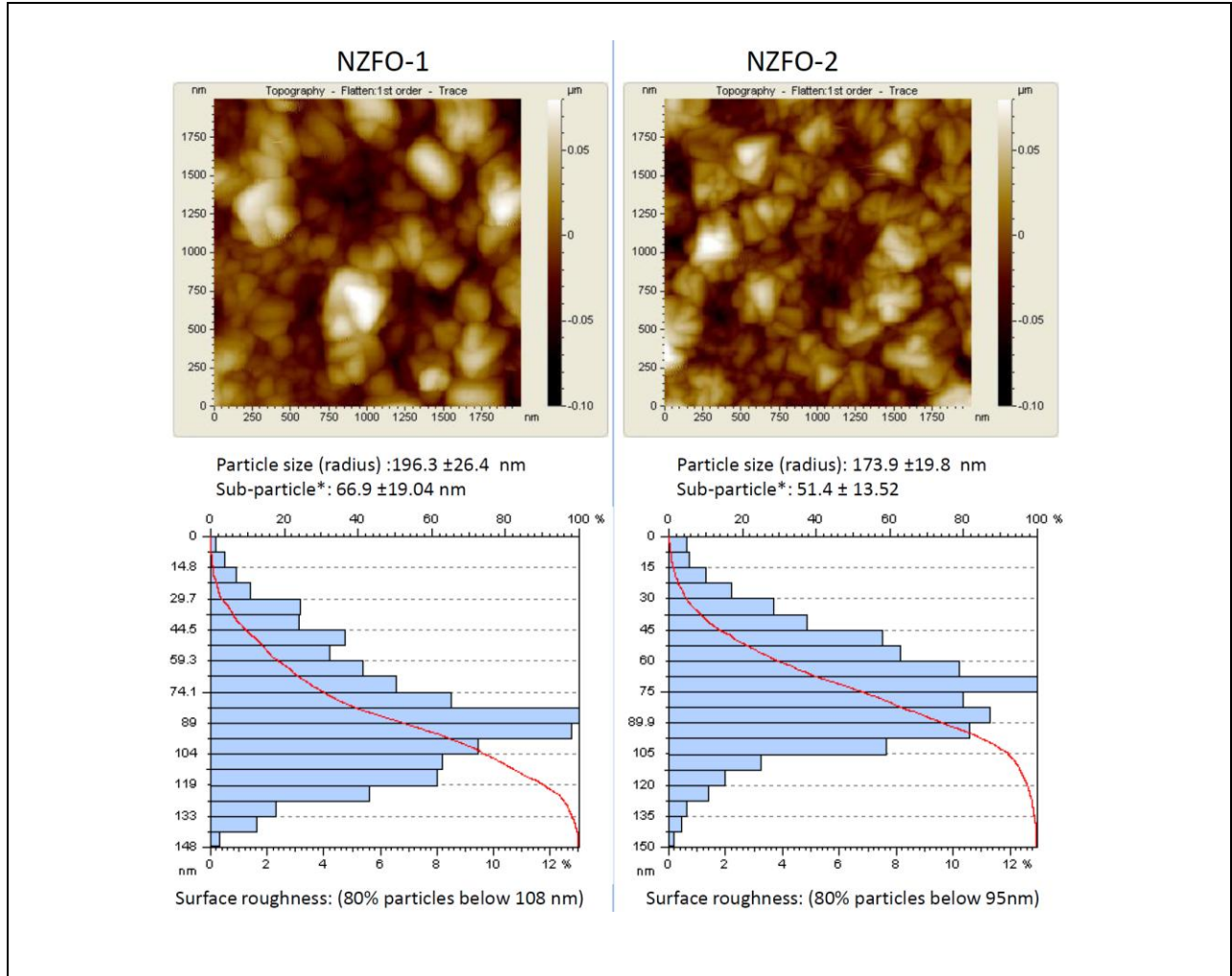

Figure 6. Surface morphology measurements of the single (top-left) and double-layer (top-right) NZFO. The size distribution of particles of single (bottom-left) and double-layer (bottom-right) are estimated by assuming a spherical shape.

For comparison, Fe_3O_4/Photoresist (PR)/Fe_3O_4 multilayer films were deposited and measured in figure 6. The thin layer of photoresist (PR) was deposited by spin coating. Fe_3O_4/PR/Fe_3O_4 sandwich structures and Fe_3O_4 single layers with constant thickness were made

on glass substrates. Figure 7 shows the measurements of Fe_3O_4/Photoresist (PR)/Fe_3O_4 multilayer films.

	Fe3O4	Fe3O4/PR/Fe3O4	(Fe3O4/PR)x4
Particle radius (um, assuming spherical shape)	2.23 ± 0.43 1.63±0.24 (sub-particles*)	2.16 ± 0.55	6.34 ± 1.95 (big clusters*) 1.49±0.56 (small particles*)

Figure 7. Surface morphology measurements of the single (left), double (middle) and multiple (right) Fe_3O_4/Photoresist (PR)/Fe_3O_4 stack.
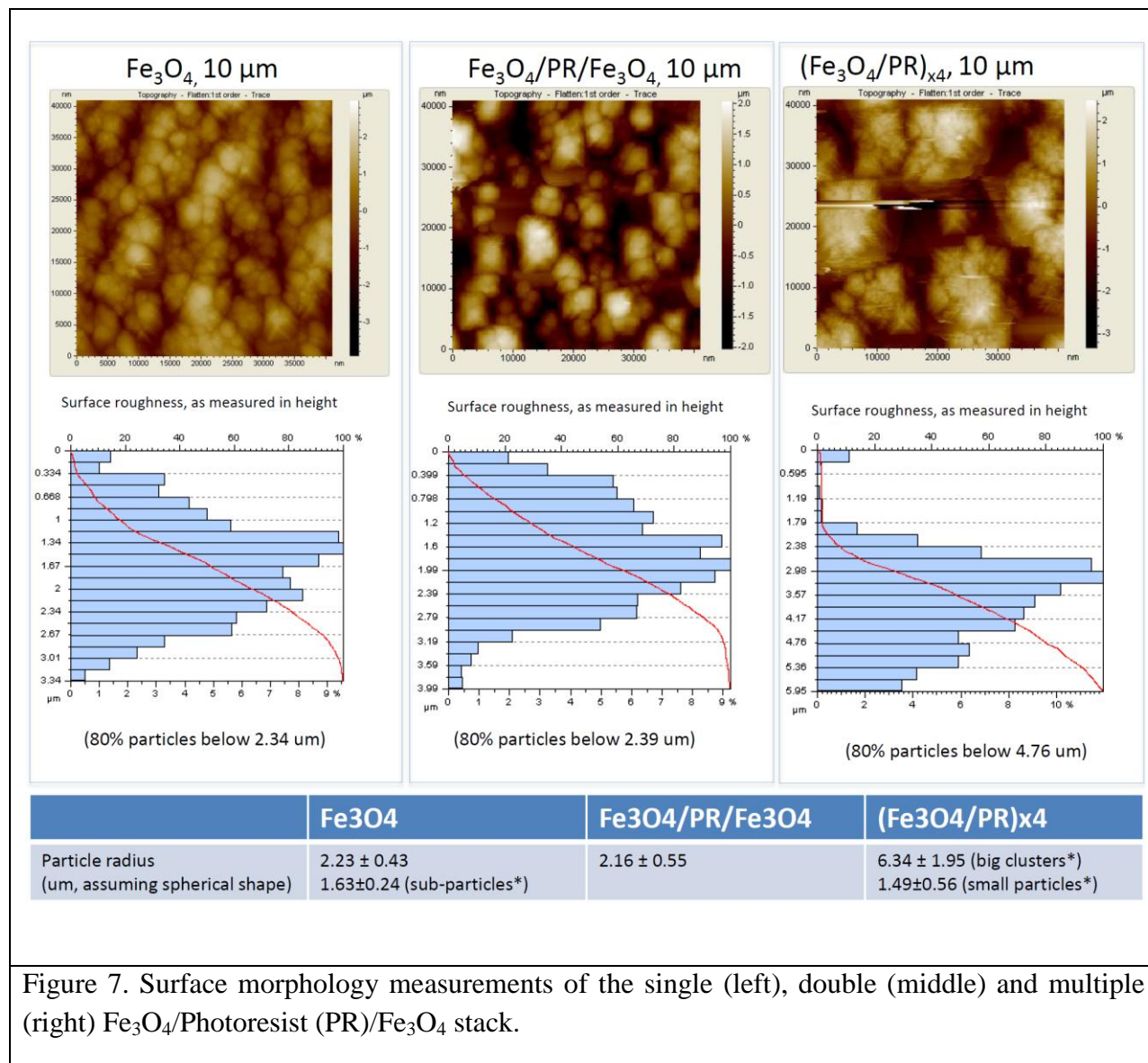
4. Support collaborations with Wright-Patterson Air Force Base

The system purchased via the DURIP program triggers and provides strong supports to a number of collaborations between Wright State University and Wright-Patterson air force base. The AFM (Fig. 8) has been used to characterize surface morphology of single atomic layer graphene

film grown by sublimation of silicon from crystalline SiC substrate (collaborated with AFRL/RXPS). Specifically, the modified SMM by combining the AFM with the network analyzer provides the unique capability to monitor the electrical property of the ultra-thin graphene film. In addition, the AFM has been used to support developing soft ferromagnetic thin films for high quality RF inductive components (collaborated with the sensor directory, AFRL).
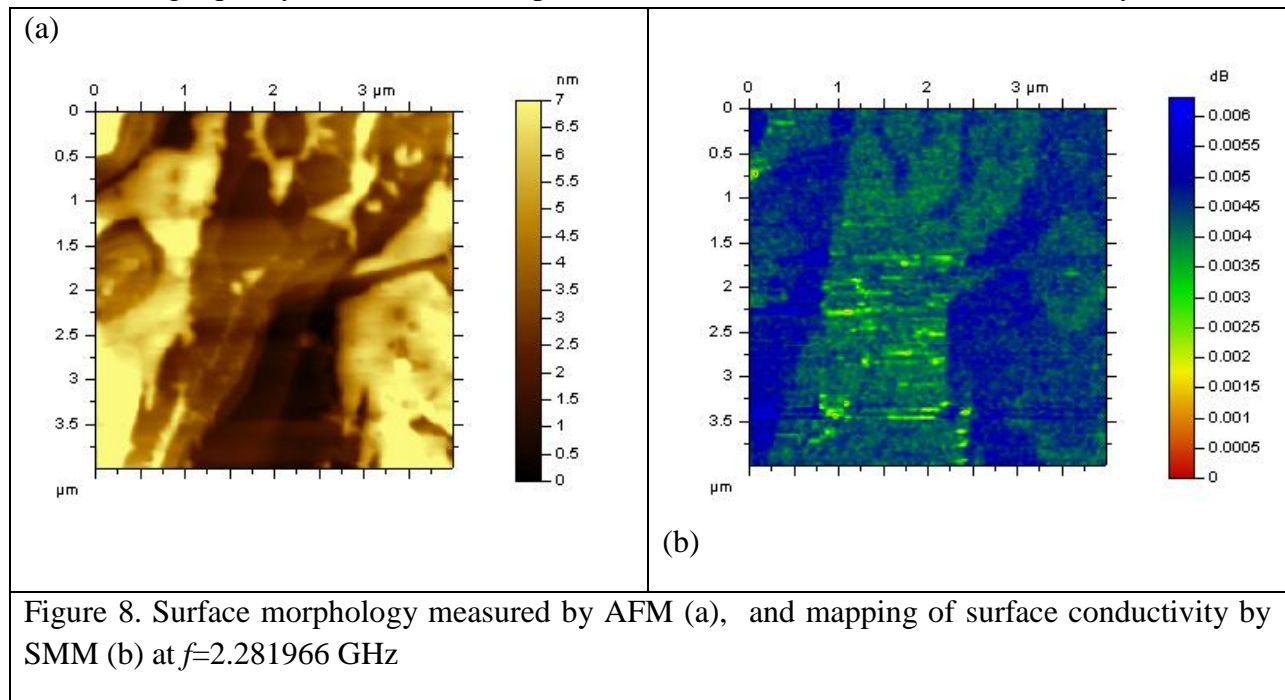
(a)

(b)

Figure 8. Surface morphology measured by AFM (a), and mapping of surface conductivity by SMM (b) at f=2.281966 GHz
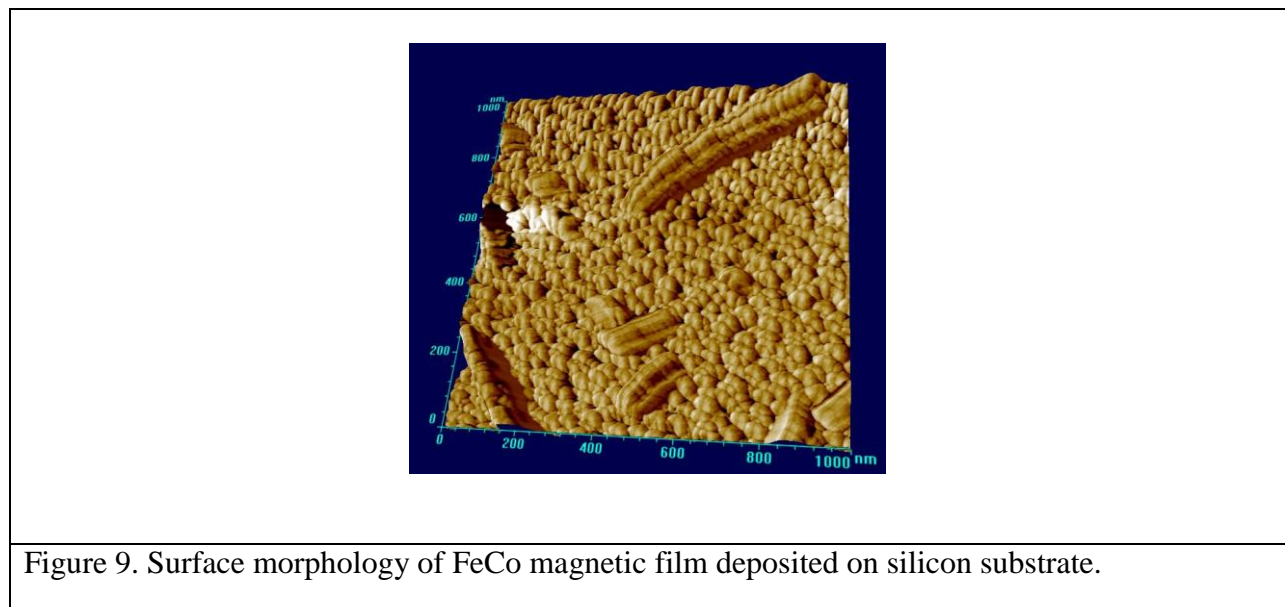
Figure 9 shows the surface morphology of FeCo magnetic film deposited at. The FeCo film exhibits the highest saturation magnetization (~2.4 Tesla).

Figure 9. Surface morphology of FeCo magnetic film deposited on silicon substrate.

5. Analysis of Dragonfly in Reverse Horizontal Take-Off and Hovering Flight

After reviewing a several series of images from an adult dragonfly in reverse horizontal take-off and hovering flight several key characteristics were determined. While there is some variation between species of dragonflies in mass and wing size, the dragonfly, in general, appears to be scalable.

The first in the series of images that was analyzed was the series in which reverse horizontal take-off was present. We characterize horizontal take-off as the gait in which the insect separates from the surface in which it was at rest in a motion in the posterior direction. A small succession of the images that were analyzed is shown in Figure 10.
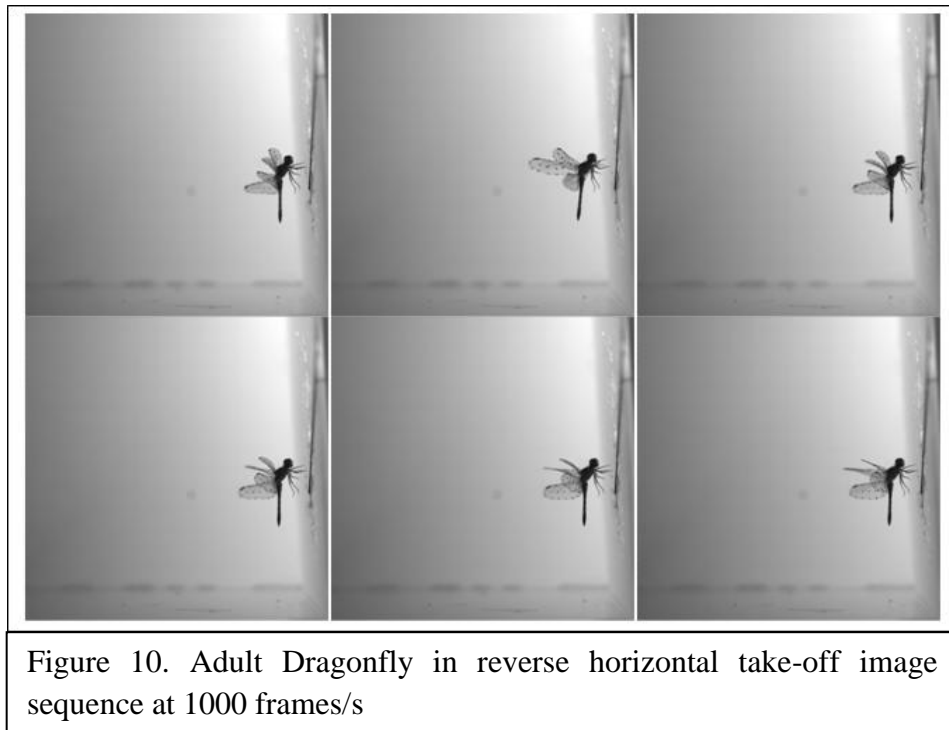
Figure 10. Adult Dragonfly in reverse horizontal take-off image sequence at 1000 frames/s

The insect appears to approach wing stroke amplitude of approximately 130 degrees with the tips of the wings nearly meeting one another behind the insect's dorsal side. The fore and hind wings appear to be less than 45 degrees out of phases with one another. The insect also appears to be flapping its wings at approximately 30 beats per second. These are all important characteristics to take note of for the insect's flight.

The next in the series of images that was analyzed was the series in which hovering flight was present. We characterize hovering is the gait in which the insect's body appears to remain stationary, or with minimal change in position and rotation, for several wing beats. A small succession of the images that were analyzed is shown in Figure 11.

Figure 11. Adult Dragonfly in hovering motion image sequence at 1000 frames/s

The insect appears to approach wing stroke amplitude of approximately 130 degrees with the tips of the wings nearly meeting one another behind the insect's dorsal side. This is the same measurement that was evident in reverse horizontal take off. The fore and hind wings appear to be further out of phase than that of reverse horizontal take off. For this gait, the wings appear to approach a phase difference of nearly 90 degrees. The insect also appears to be flapping its wings at an increased rate, approximately 35 beats per second.

By comparing the two modes of flight we can see that for horizontal takeoff, the insects' fore and hind wings are more in-phase with one another and the flapping frequency has been slightly reduced from that of hovering. For hovering flight, it is evident that the insect's wings are nearly completely out of phase with one another. It suggests that flight speed and gait are in direct correlation with phase relationship. This is an interesting aspect to take into consideration in the design of a quad-wing MAV. If a skilled flying insect such as the dragonfly uses phase relationship manipulation between various gaits of motion, then there must be an evolutionary reason for such a characteristic. For further investigation of how phase relationship plays a role in lift production, more quantitative analysis must be performed.

Another characteristic that seemed to vary for different gaits was the flapping frequency of the wings. Because the relative stroke amplitude seems to be the same in nearly all forms of flight, the frequency of stroke is clearly an independent variable in lift production. It has been proposed that flight performance is in direct correlation with flapping frequency. By performing

more quantitative analysis of varying flapping frequencies, we can hope to further understand how flapping frequency plays a role in lift generation.

It is also note worthy the wing shape throughout various modes of flight. Unlike conventional aircraft, insects' wings act as deformable membranes, changing shape throughout the stroke in all forms of flight. This is yet another aspect of evolution that needs further investigation to understand why it is present in nearly all species of insects.

6. Advanced Data Analysis of High-Speed Images

a. 3-D Surface Reconstruction Using High-speed Images

Prior to photographing, the dragonfly's wings were marked in a grid pattern with black ink in order to provide anchor points to aid in reconstructing their 3D shape as they deform while flapping. The initial 3D wings and body were generated with Catmull-Clark subdivision surfaces using Autodesk Maya by aligning vertices corresponding to the first level of the subdivision
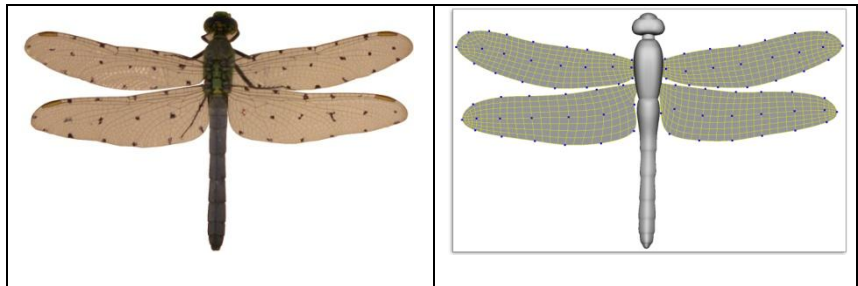

Figure 12. Corresponding reconstructed wings and body of the dragonfly, real one and models of wing and body.

surface hierarchy with the anchor points on the wings. Figure 12 shows the initial configuration of the wings and body based on the dragonfly in Figure 12.

The wings were then animated with key frame animation by repeating the anchor point based alignment process along each axis at each time step of the images of the flying dragonfly taken with the high speed camera's. Since anchor points are available on both the interior of the wing and the edges, an approximation of the true 3D shape of the wings as they bend and twist is captured with the smooth subdivision surface representation. In frames where the wings rotate such that the location of the anchor points along one or more axes is not discernable, reconstructions were performed at adjacent frames and spline interpolation was used to estimate anchor point location at the unclear frame. Figure 13 shows an example of how the 3D wing models were aligned to the images taken from the high speed cameras at a single time step during slow flight. The dragonfly's body was assumed to be rigid and was animated by aligning its outer border to the silhouette of the body in the images, however the body moves very slowly compared to the wings, so its reconstruction is trivial in comparison.
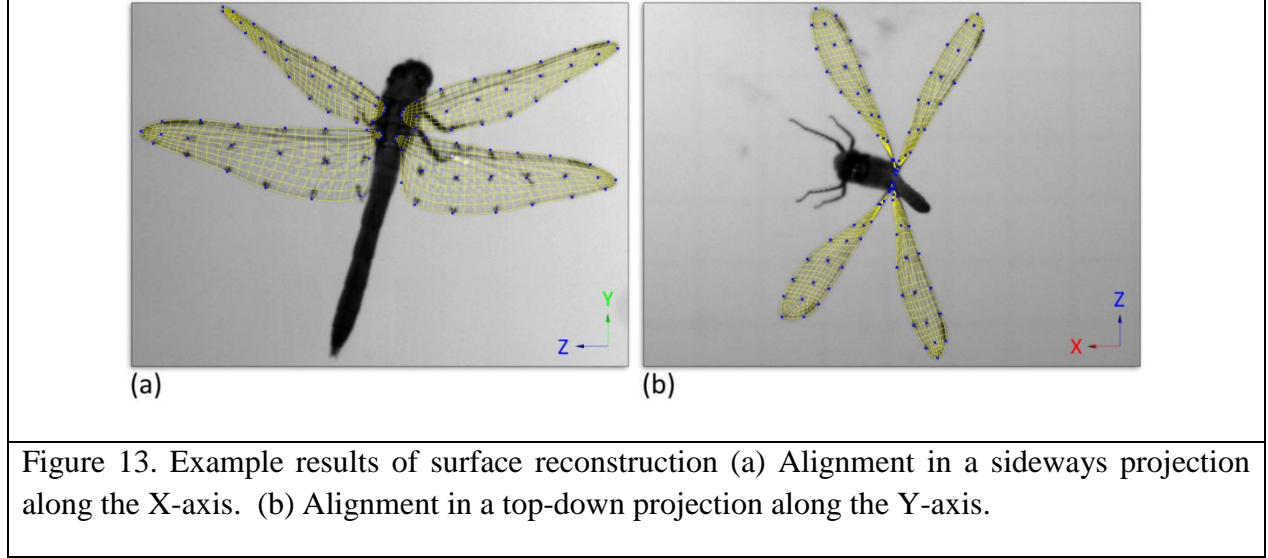
Figure 13. Example results of surface reconstruction (a) Alignment in a sideways projection along the X-axis. (b) Alignment in a top-down projection along the Y-axis.

b. Singular Value Decomposition (SVD) of the Dragonfly Wing Kinematics

SVD is more general than eigenvalue decomposition and intimately relates to the matrix rank and reduced-rank least-squares approximation. In the SVD approach a function $A(x,t)$ can be expressed as,

$$A(x,t) = \sum_{i=1}^{M} a_i(t)\phi_i(x)$$

where x is the spatial coordinate and t is the time, $a_i(t)$ are the eigenvalue coefficients and $\phi_i(x)$ are the eigenvectors. Using SVD, a data matrix can be decomposed as:

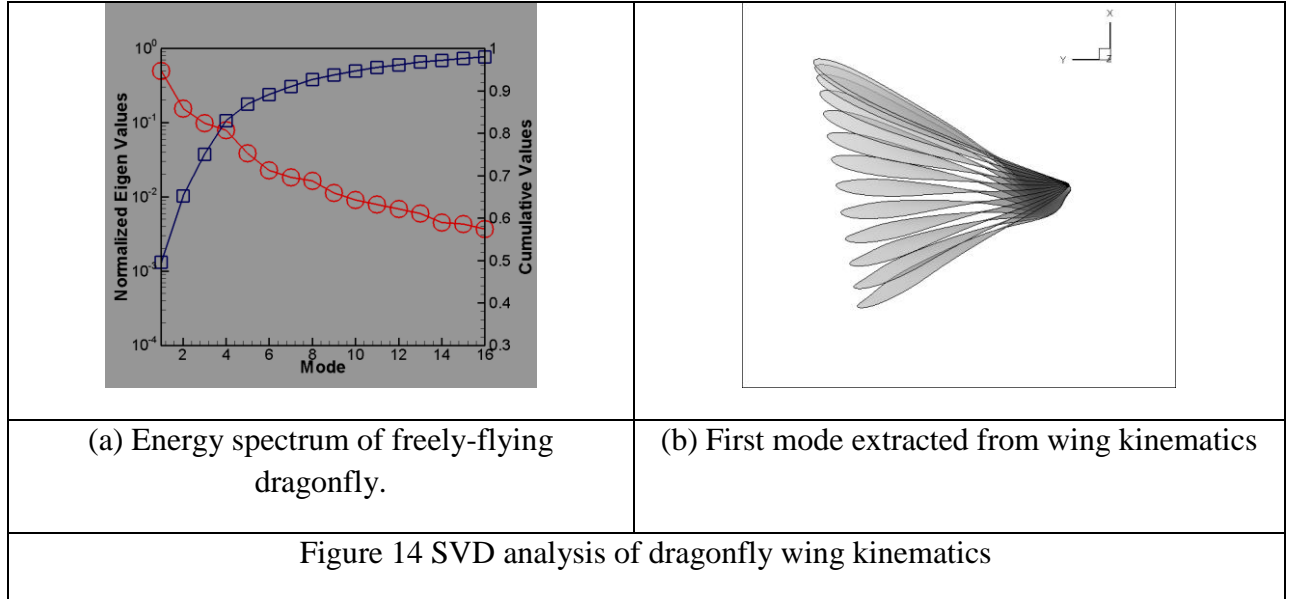$$[A]_{n \times m} = [U]_{n \times n}[S]_{n \times m}[V]_{m \times m}^T$$

where $[U]_{n \times n}$ and $[V]_{m \times m}^T$ are two orthogonal column matrices, n is the number of data set and m is the number of data points in each set. $[S]_{n \times m}$ is a matrix where all elements are zero except along the diagonal. The diagonal values are called the singular values of $[A]$ (and also $[A]^T$) and are unique. The diagonal elements S_{ii} consist of $r = \min(n,m)$ nonnegative numbers, which are arranged in descending order. They can be interpreted as the weight contribution of each mode into POD reconstruction. The S_{ii} values are indeed the square roots of the eigenvalues of AA^T (or A^TA), where the eigenvectors of AA^T make up the columns of $[U]$, while the eigenvectors of A^TA make up the columns of $[V]$. If one considers only the first N energetic modes of the system ignoring the rest, the POD-based approximation for the data set becomes:

$[A]_{N \times m} = [U]_{N \times N}[S]_{N \times m}[V]_{m \times m}$

In our case, $[U]$ represents the change of each mode with time, singular values are the weight contribution of each mode and $[V]$ contains the eigenvectors corresponds to the spatial distribution of the modes. As it is stated earlier, SVD method is employed for the POD analysis of dragonfly wing kinematics which was described by 45 distinct timeframes in one fin-beat cycle. For the POD analysis, surface data is interpolated to represent each frame by 865 nodal points. The function which defines wing kinematics is a displacement vector $(\Delta x, \Delta y, \Delta z)$ in the three dimensional space. Displacements taken by every node on the wing surface at each of the time-frames are inserted into a matrix $[A]$ in a coupled manner as:

$$
A = \begin{bmatrix}
\Delta x_1(t_1) & \Delta y_1(t_1) & \Delta z_1(t_1) & \dots & \Delta x_{865}(t_1) & \Delta y_{865}(t_1) & \Delta z_{865}(t_1) \\
\Delta x_1(t_2) & \Delta y_1(t_2) & \Delta z_1(t_2) & \dots & \Delta x_{865}(t_2) & \Delta y_{865}(t_2) & \Delta z_{865}(t_2) \\
\vdots & \vdots & \vdots & \vdots & \vdots & \vdots & \vdots \\
\Delta x_1(t_{44}) & \Delta y_1(t_{44}) & \Delta z_1(t_{44}) & \dots & \Delta x_{865}(t_{44}) & \Delta y_{865}(t_{44}) & \Delta z_{865}(t_{44})
\end{bmatrix}_{44 \times 2595}
$$

Matrix $[A]$ is then subject to SVD analysis which leads to 44 singular values. The normalized singular value spectrum of the wing kinematics is shown in figure 14(a) along with a cumulative plot for the same data. The singular values are normalized by the sum of all singular values whereas the cumulative values rescale so that they sum to unity. A number of interesting observations can be made from this plot. First, the singular value spectrum shows three distinct ranges: the first between Mode-1 to -5 where we see a rapid decrease in the amplitude, the second from Mode- 5 to -11 where there is a much slower reduction in amplitude and finally the range from Mode-12 to 19 which has negligible contribution. The rapid initial decrease in the

(a) Energy spectrum of freely-flying dragonfly.	(b) First mode extracted from wing kinematics

Figure 14 SVD analysis of dragonfly wing kinematics

spectrum is interesting in that it suggests that a small number of modes contain most of the essential features of the wing motion. In fact, the cumulative values show that the first two, three and five modes capture 62%, 73% and 85% respectively of the total motion. The first mode of

the wing kinematics is projected on x-y plane and is shown in Fig. 14(b), in which it looks like a flapping motion around vertical axis.

c. Euler Angle Analysis and Study of Wing Motions

Given the laboratory coordinates of the dragonfly, a set of Euler angles describing the rotation sequence from the laboratory-fixed frame XYZ to the body-fixed frame X'Y'Z' is possible to compute. It is always necessary to have the body-fixed frame X'Y'Z' for the researchers to identify the stroke plane angle of the dragonfly's wings, moreover, the downstroke and upstroke of wing beat. Being a kind of Euler angles widely used in aerospace, yaw, pitch and roll describe the rotations of the dragonfly's body in Euler angles form of z-y-x, i.e. (1) rotation about the Z-axis by yawing angle Ψ; (2) rotation about the new Y- axis by pitching angle Θ; (3) rotation about the new X-axis by rolling angle Φ (as shown in Figure 15(b)).
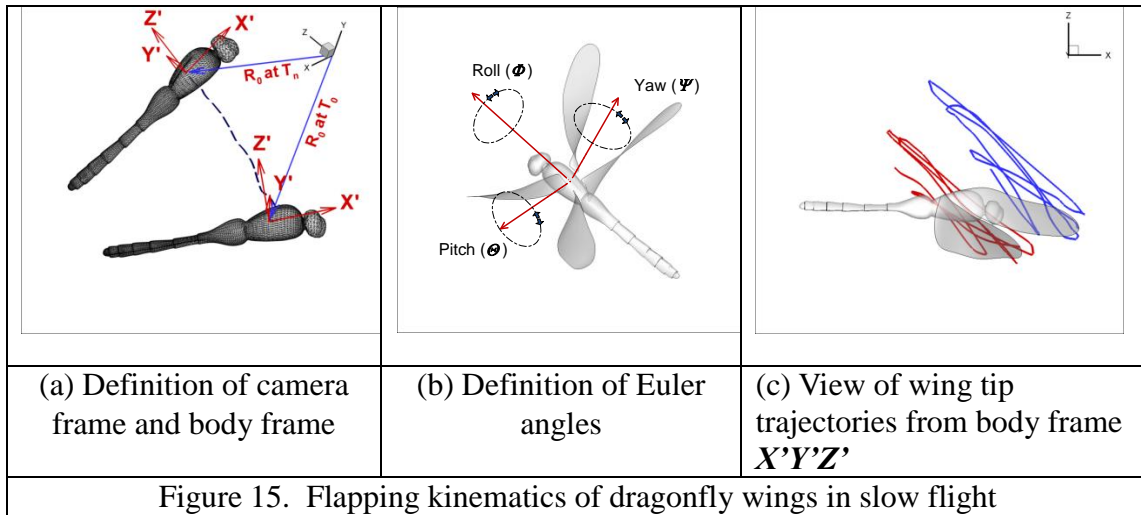
The relation between Camera Frame *XYZ* and Body Frame *X'Y'Z'* which attached to body is

$$R = T^{-1}r + R_0$$

where

- $R_0 = (R_x, R_y, R_z)$: the vector from *XYZ* to *X'Y'Z'*
- $r = (x,y,z)$: any point in *X'Y'Z'* frame
- R: the coordinates of r in *XYZ* frame

After transforming from camera frame to body frame (Figure 15(a)), the Euler angles of body motion can be determined as Figure 15(b) and wing tip trajectories relative to wing body can will easily observed, too. Figure 15(c) shows the wing stroke plane inclination to the body axis.

(a) Definition of camera frame and body frame	(b) Definition of Euler angles	(c) View of wing tip trajectories from body frame *X'Y'Z'*

Figure 15. Flapping kinematics of dragonfly wings in slow flight

Here, matrix T is equal to

$$T = B \bullet C \bullet D$$

where

$$D(\Psi) = \begin{pmatrix} Cos[\Psi] & Sin[\Psi] & 0 \\ -Sin[\Psi] & Cos[\Psi] & 0 \\ 0 & 0 & 1 \end{pmatrix} \quad C(\theta) = \begin{pmatrix} Cos[\theta] & 0 & -Sin[\theta] \\ 0 & 1 & 0 \\ Sin[\theta] & 0 & Cos[\theta] \end{pmatrix} \quad B(\Phi) = \begin{pmatrix} 1 & 0 & 0 \\ 0 & Cos[\Phi] & Sin[\Phi] \\ 0 & -Sin[\Phi] & Cos[\Phi] \end{pmatrix}$$

Select *(x,0,0), (0,y,0)* in the body-fixed frame X'Y'Z' and plug into above equation. We are able to get the angles of yaw, pitch and roll by

$$\theta = \arcsin(\frac{z_1 - R_z}{-x})$$

$$\psi = \arccos(\frac{x_1 - R_x}{x\cos\theta})$$

$$\phi = \arcsin(\frac{z_2 - R_z}{y\cos\theta})$$

In mathematics, there exist singularities in the Euler angle parametrization, in which a degree of freedom is lost, e.g. $\theta = \frac{\pi}{2}$ or $-\frac{\pi}{2}$. This doesn't happen in current studies because it is hardly to observe a dragonfly flying in a free mode where the pitching angle of its body is exactly vertical.

The range of motion for the fore and rear wings on the dragonfly can be seen in Table 1 and key descriptors are depicted in Figure 16. This range of motion and phase difference will be a constraint in the design. The equation used to find the motion for the hind wings at any given time can be given as:

$$\varphi_h = \frac{\Phi_h}{2}\cos(\omega_h t + \delta_h) + (\Phi_{h,0} + \frac{\Phi_h}{2})$$

where ω_h represents the angular frequency and δ_h is the phase. The equation for the front wings at any given time is shown below:

$$\varphi_f = \frac{\Phi_f}{2}\cos(\omega_f t + \delta_f) + (\Phi_{f,0} + \frac{\Phi_f}{2})$$

The quad-wing design will follow the same range of motion and maintain the same phase from use of this data. The phase is calculated using the following equation:
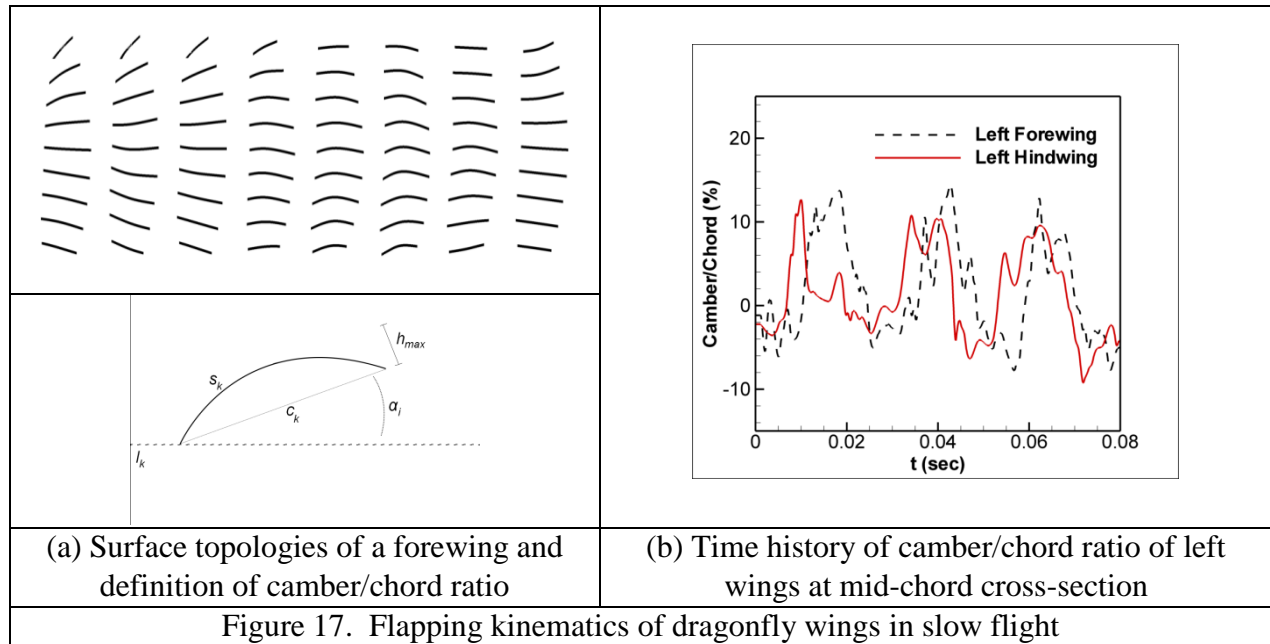
$$\Delta = \delta_h - \delta_f$$

Hind	Locates Range of Motion… $\Phi_{h,0}$	76°	
	Range of Motion… Φ_h	51°	
	Phase… δ_h	180°	
	Stroke Plane Inclination… γ_h	33.3°	
Fore	Locates Range of Motion… $\Phi_{f,0}$	40°	
	Range of Motion… Φ_f	99°	
	Phase… δ_f	119°	
	Stroke Plane Inclination… γ_f	37.9°	
Phase Difference… Δ		61°	
Flight Path Angle… θ		-10°	
Body Attitude Angle… β		-25°	
Frequency… f		33 Hz	

Table 1 Key Descriptors of flapping flights	Figure 16 Wing Stroke plane with Respect to Angle of Attack

d. Wing Deformation and Surface Topologies

(a) Surface topologies of a forewing and definition of camber/chord ratio	(b) Time history of camber/chord ratio of left wings at mid-chord cross-section
Figure 17. Flapping kinematics of dragonfly wings in slow flight	

Wing surface deformation and topologies are visualized in Figure 17 based on the time series wing surface reconstruction. The camber/chord ration in Figure 17(a) is defined by the

ratio of maximum chamber height and wing chord. As plotted in Figure 17(b), time history of the camber/chord ratio of left-side wings show the maximum ratio is about 12% and there is phase shift between hind wings and forewings.

e. CFD Simulation

A second-order finite-difference based immersed-boundary solver has been developed which allows us to simulate flows with complex immersed 3-D moving bodies. The method employs a second-order central difference scheme in space and a second-order accurate fractional-step method for time advancement. The Eulerian form of the Navier-Stokes equations are discretized on a Cartesian mesh and boundary conditions on the immersed boundary are imposed through a "ghost-cell" procedure. For this particular simulation of dragonfly in free flight, comprehensive grid and domain size independence studies have also been conducted. Based on these studies, a domain size of $30\times30\times30$ and a $209 \times 193 \times 241$ grid has been chosen for all 3-D simulations.
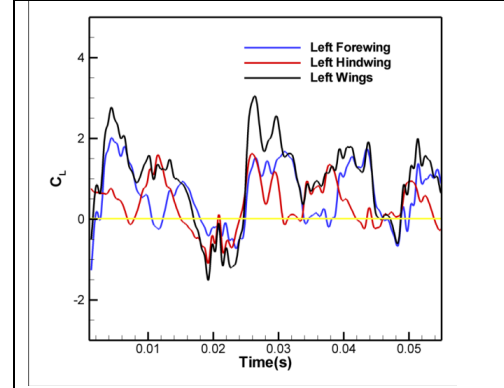

Figure 18. Time history of lift coefficient over the first two strokes.

Figure 19 shows the time sequence of the direct numerical simulation of the dragonfly in take-off motion. The isosurfaces of the eigenvalue imaginary part of the velocity gradient tensor $\partial u_i / \partial x_j$ are plotted in order to clearly show the vortex topology. Leading-edge vortices can be observed in the plot. The key feature observed here is the presence of vortex rings and wing-wake interactions. The following step will investigate the associated force production.

| $t = 0.004s$ | $t = 0.008s$ |

t = 0.012s	*t = 0.016s*
Figure 19. Wake structures of a dragonfly in take-off motion.	
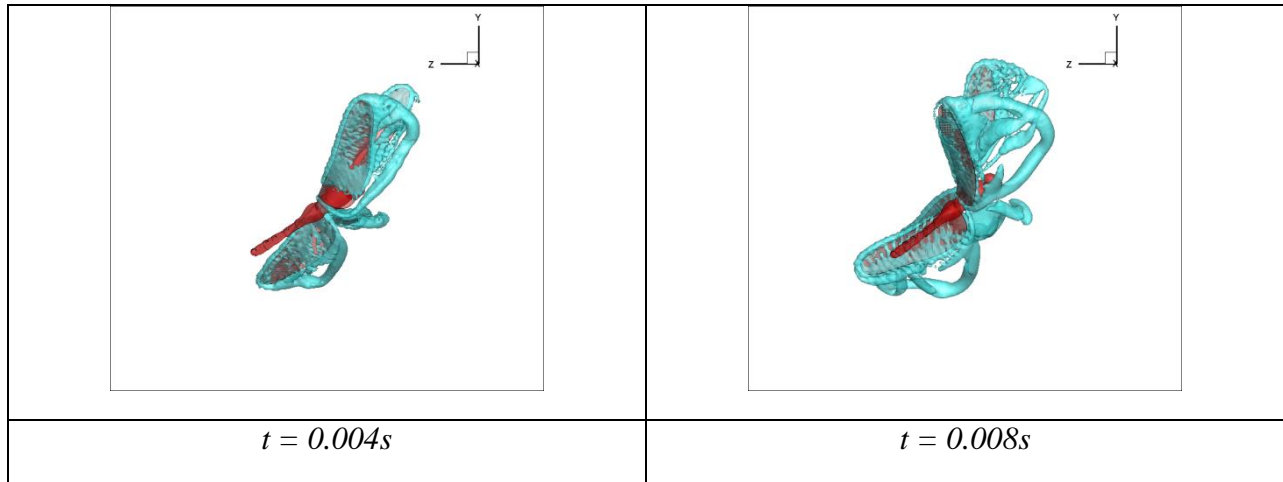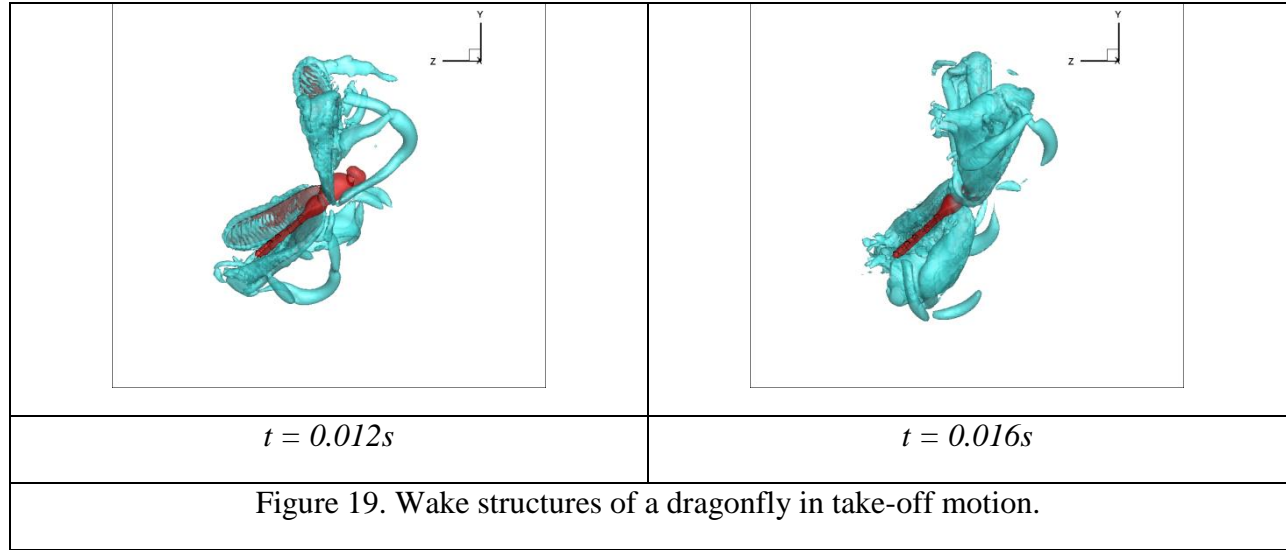
7. Publications related to the grant

   a. S. L. Cheekati, Y. Xing, Y. Zhuang, and H. Huang, "Lithium Storage Characteristics in Nano-Graphene Platelets", accepted for publication at Materials Challenges in Energy

   b. O. Obi, M. Liu, G. Yang, J. Lou, X. Xing, Z. Cai, S. Liang, Z. Agranat, S. Stoute, K. S. Ziemer, Y. Xing, Y. Zhuang, and N. X. Sun, "Spin-Spray Deposited Ferrite/Non-Magnetic Multilayer Films with Enhanced Microwave Magnetic Properties", under review, *IEEE Trans.Magn.,* Oct. 2010.

   c. Iramnaaz, T. Sandoval, Y. Xing, K. Xue, Y. Zhuang, and R. Fitch, "Graphene based RF/microwave impedance sensing of DNA", Abstract accpeted by 61th IEEE Electronic Components and Technology Conference, May, 2011

   d. T. Sandoval, H. Schellevis, B. Rejaei, Y. Zhuang, "Ultra-high Quality Factor RF Inductors using Low Loss Conductor Featured with Skin Effect Suppression", Abstract accpeted by 61th IEEE Electronic Components and Technology Conference, May, 2011

   e. Y. Xing, H. Huang, and Y. Zhuang, "Differential Charge Transfer Characteristics of Graphene for Impedance-based Biosensing", Abstract accepted by MRS 2010 Fall

   f. Dong, H., Z. Liang, H. Wan, and C. Koehler "Computational Modeling and Analysis of Aerodynamics of Deformable Dragonfly Wings", in preparation to submit to *Journal of Fluid Mechanics*, 2010.

   g. Z. Liang, C. Koehler, H. Dong, Z. Gaston, H. Wan, "Wing Deformability and Surface Topographies of Free-flying Dragonflies", in preparation to submit to *Journal of Experimental Biology*, 2010.

   h. Dong, H., Z. Liang, C. Koehler, and H. Wan, "Wing Flexion and Associated Aerodynamic Performance in Dragonfly Take-off Flight ", in preparation to submit to *Bioinspiration & Biomimetics*, 2010.

i. Dong, H., C. Koehler, Z. Liang, H. Wan, and Z. Gaston (2010). An Integrated Analysis of a Dragonfly in Free Flight. 40th AIAA Fluid Dynamics Conference and Exhibit, AIAA-2010-4390.

8. Theses/Dissertations Associated with Grant

   a. "Graphene based bio-sensing," I. Iramnaaz, Master thesis, June 2010 – present, expected graduation: March 2011.
   b. "Nano-granular magnetic meta-materials for high quality RF passive components," T. Sandoval, Master thesis, June 2009 – present, expected graduation: Dec. 2010.
   c. "Computational Analysis of Vortex Structures in Flapping Flights" Zongxian Liang, Ph.D. Dissertation, 2007 June – Present, oral defense June 2010, expected graduation: June 2011.
   d. "Motion Tracking and Fluid Dynamics in Bio-inspired Flights," Yan Ren, Master thesis, March 2010 – present, expected graduation: June 2011.
   e. "Vortex-Dominated Flows in Massively-Unsteady Low Reynolds Number Aerodynamics," Richard Martin, Master thesis, June 2010 – present, expected graduation: June 2011. (AFRL/DAGSI student).
   f. "Flight Dynamics in Insect Maneuvering Flights", Samane Zeyghami, Ph.D. dissertation, Sept 2010 - present, expected graduation: December 2014.

9. Senior Design and Independent Projects

   a. Winter and Spring, 2010, Dominic Mozel, Larry Schimmoeller, Joenell Rosales, "Microwave imaging".
   b. Winter and Spring, 2009, James Blair and Travis Burnette, "Piezoelectric materials based actuator for MAVs".
   c. Winter and Spring, 2009, Brian S. Marshall, "Micro aerial vehicles".
   d. Fall 2010, Zach Votaw "Study of flexible tail aerodynamics".
   e. Fall 2010, Adam Harp, "Redesign a gearbox for motor-driven actuation system".
   f. Fall 2010, Aswanth Kumar, "Design a flexible wing for motor-driven actuation system".
   g. Summer 2010, Conrad Jett, "Design an actuation system for flapping flight".
   h. Spring 2010, Girish Byrappa, "Modeling and Testing of a modeled dragonfly wing."
   i. Fall 2009, Zach Gaston, "Data aquisation of a high-speed photogrammetry system".
   j. Fall 2009, Girish Byrappa, "Structure analysis of a modeled dragonfly wing."
   k. Fall 2010, Winter 2011, Zach Gaston, Phillip Cooley, "Design a simple and durable actuator for flapping wing MAVs".
   l. Winter 2010, Spring 2010, Richard Martin, Asela Benthara, Adam Harp, Conrad Jett, Matthew Mills, Wesley Moosman, Joe Parsley, Cody Wright, Zachary

Votaw, Andy Walker, Aron Brezina, Adam Mayes, "Design of a Bio-inspired Flapping-Wing Micro Air Vehicle Actuator: Wing Design, Actuation Design, and System Design", **totally three teams**, supported by **AFRL CAPSTONE senior project**.

m. Fall 2009, Winter 2010, Matt Maples, Adam Gualtieri, "Design of a Bio-inspired Quad-winged Micro Air Vehicle".

10. Media Report, Honors & Awards Received

Title	Media	Dates
A Spy on the Wall	Composites Manufacturing	Winter 2009
Small Aircraft Will Mimic Dragonfly	Red Orbit	Nov 2010
Using CFD Visualization To Study the Complex Flow Physics of Dragonfly Flight	Tecplot Contours Newsletter	December 2009
The Latest Trend in Aircraft: Really, Really Tiny	Discover Magazine	March 4, 2010
Tecplot Provides a View to MAV Flight: Researchers use CFD analysis and Tecplot visualization to map the flight of dragonflies from development of micro air vehicles	Desktop Engineering Magazine	April 2010
Biomimicary: Flexible Flyer	American Society for Engineering Education, PRISM	April 2010
The Bug in Our Backyard - Wright State Students Help Creating a Flying Robot	Dayton City Paper	June 2010
Presidential Award for Faculty Excellence: Early Career Achievement	Wright State University	2010
Early Career Achievement Award	College of Engineering and Computer Science, WSU	2010